

# Chemical Features in the Circumnuclear Disk of the Galactic Center ★ ★ ★

N. Harada<sup>1,2</sup>, D. Riquelme<sup>1</sup>, S. Viti<sup>3</sup>, I. Jiménez-Serra<sup>3,4</sup>, M. A. Requena-Torres<sup>1</sup>, K. M. Menten<sup>1</sup>, S. Martín<sup>5,6</sup>, R. Aladro<sup>6,7</sup>, J. Martín-Pintado<sup>8</sup>, and S. Hochgürtel<sup>1</sup>

<sup>1</sup> Max Planck Institute for Radio Astronomy, Auf dem Hugel 69, D-53121 Bonn, Germany

<sup>2</sup> Academia Sinica Institute of Astronomy and Astrophysics, No.1, Sec. 4, Roosevelt Rd, Taipei 10617, Taiwan, R.O.C.

<sup>3</sup> University College London, Gower Street, London, WC1E 6BT, UK

<sup>4</sup> European Southern Observatory, Karl-Schwarzschild-Str. 2, D-85748 Garching, Germany

<sup>5</sup> Institut de Radio Astronomie Millimétrique, 300 rue de la Piscine, Dom. Univ., F-38406, St. Martin d'Hères, France

<sup>6</sup> European Southern Observatory, Avda. Alonso de Córdova 3107, Vitacura, Santiago, Chile

<sup>7</sup> Department of Earth and Space Sciences, Chalmers University of Technology, Onsala Observatory, 439 92 Onsala, Sweden

<sup>8</sup> Centro de Astrobiología (CSIC-INTA), Ctra. de Torrejón Ajalvir km 4, E-28850 Torrejón de Ardoz, Madrid, Spain

Received .../ Accepted ...

## ABSTRACT

**Aims.** The circumnuclear disk (CND) of the Galactic Center is exposed to many energetic phenomena coming from the supermassive black hole Sgr A\* and stellar activities. These energetic activities can affect the chemical composition in the CND by the interaction with UV-photons, cosmic-rays, X-rays, and shock waves. We aim to constrain the physical conditions present in the CND by chemical modeling of observed molecular species detected towards it.

**Methods.** We analyzed a selected set of molecular line data taken toward a position in the southwest lobe of the CND with the IRAM 30m and APEX 12-meter telescopes and derived the column density of each molecule using a large velocity gradient (LVG) analysis. The determined chemical composition is compared with a time-dependent gas-grain chemical model based on the UCL\_CHEM code that includes the effects of shock waves with varying physical parameters.

**Results.** Molecules such as CO, HCN, HCO<sup>+</sup>, HNC, CS, SO, SiO, NO, CN, H<sub>2</sub>CO, HC<sub>3</sub>N, N<sub>2</sub>H<sup>+</sup> and H<sub>3</sub>O<sup>+</sup> are detected and their column densities are obtained. Total hydrogen densities obtained from LVG analysis range between  $2 \times 10^4$  and  $1 \times 10^6$  cm<sup>-3</sup> and most species indicate values around several  $\times 10^5$  cm<sup>-3</sup>, which are lower than values corresponding to the Roche limit, which shows that the CND is tidally unstable. The chemical models show good agreement with the observations in cases where the density is  $\sim 10^4$  cm<sup>-3</sup>, the cosmic-ray ionization rate is high,  $> 10^{-15}$  s<sup>-1</sup>, or shocks with velocities  $> 40$  km s<sup>-1</sup> have occurred.

**Conclusions.** Comparison of models and observations favors a scenario where the cosmic-ray ionization rate in the CND is high, but precise effects of other factors such as shocks, density structures, UV-photons and X-rays from the Sgr A\* must be examined with higher spatial resolution data.

**Key words.** ISM: molecules, Galaxy: center

## 1. Introduction

Located at  $d \sim 8.4$  kpc from the Sun (Reid et al. 2009), the center of the Milky Way is the nearest galactic nucleus. The supermassive black hole at its center is not currently active with an Eddington ratio of only  $10^{-9}$ , but X-ray observations suggest possible higher activity in the past (e.g., Ponti et al. 2013). Even within the central parsec, at a close vicinity of Sgr A\*, a massive star cluster is found with a total stellar mass of  $\sim 10^6 M_{\odot}$  (Schödel et al. 2009). Star formation near the black hole is difficult to explain due to tidal shear. It has been proposed that these massive stars may have formed in situ or farther away from the black hole and migrated inwards (Paumard et al. 2006, and references therein). The black hole is surrounded by the cir-

cumnuclear disk (CND) composed of molecular and atomic gas (Güsten et al. 1987). The CND is actually a ring-like structure surrounding the very central region with an inner radius of 1.5 pc ( $\sim 30$  arcsec) that extends up to 7 pc at negative Galactic longitudes (Oka et al. 2011).

Studying the molecular gas in the CND might yield information as to what extent stars can be formed in situ or not. The molecular inventory of the CND has been mapped in different tracers such as CO, CS and HCN (Serabyn et al. 1986; Lo 1986; Güsten et al. 1987). Bradford et al. (2005) found a high ( $T_{\text{kin}} \sim 200 - 300$  K) kinetic temperature of the molecular gas, and proposed shocks as the dominant heating source. Higher resolution images of the HCN and HCO<sup>+</sup> (1 – 0) lines were obtained by Christopher et al. (2005) and they concluded that the molecular gas has high enough densities to be tidally stable. On the other hand, Requena-Torres et al. (2012) conducted a multi- $J$  transition analysis of CO, and derived a much lower density of  $n_{\text{H}} \sim 6 \times 10^4$  cm<sup>-3</sup> for most of the material. Besides the study of physical conditions by above authors, Mills et al. (2013) and Smith & Wardle (2014) used multi- $J$  lines of HCN to estimate the excitation conditions of the gas. Their derived densities range

Send offprint requests to: Nanase Harada, e-mail: harada@asiaa.sinica.edu.tw

\* Figures 5-9 are only available in electronic form via <http://www.edpsciences.org>

\*\* Based on observations carried out with the IRAM 30m Telescope. IRAM is supported by INSU/CNRS (France), MPG (Germany) and IGN (Spain).

somewhere between those derived by Christopher et al. (2005) and Requena-Torres et al. (2012). Martín et al. (2012) explored the chemical complexity by mapping CN, SiO, H<sub>2</sub>CO, HC<sub>3</sub>N in the CND. Recently, a line survey in the CND of the 3mm wavelength range was conducted by Takekawa et al. (2014).

Probing the physical conditions of molecular material is a complex problem. The abundance of a molecule may be influenced by a variety of phenomena. Moreover, even for a *given* molecule, different transitions with different frequencies and intrinsic strengths may require a wide range of critical densities for their excitation. In turn, analysis of multi-transition datasets with, e.g., a large velocity gradient (LVG) analysis using a radiative transfer program may yield estimates of the kinetic temperature and density. In general, it is necessary to observe a variety of molecules as wide as possible over the broadest feasible frequency range. Riquelme et al. (in preparation) conducted a line survey using the IRAM 30 meter telescope towards a position in the southwest lobe of the CND, covering 80 to 115 GHz and 129 to 175 GHz. Hochgürtel (2013, PhD thesis) surveyed a similar region using the FLASH+ receiver (Klein et al. 2014) on the APEX 12-meter telescope (270 to 379 GHz and 385 to 509 GHz; Güsten et al. 2006). Based on their results, this paper studies possible interpretations of the chemical features observed in the CND.

In section 2, we discuss the processes that can affect the CND's physical conditions and chemistry. Column densities from the LVG analysis are presented in Section 3. The details of the chemical model are presented in Section 4, while we discuss the results of the chemical modeling in Section 5. The interpretation of the results is discussed in Section 6, and main results are summarized in Section 7.

## 2. Physical conditions and the heating of the CND

In this section we summarize the environment within and surrounding the CND that can affect the chemical composition of the molecular gas. Ionizing sources such as UV-photons, cosmic rays, and X-rays can all dissociate molecules as well as heat the gas. Shock waves may also provide very efficient heating. Fast shocks also ionize the gas. These factors are also dependent on the density distribution of the molecular clump.

### 2.1. Kinetic Temperature and Heating Mechanisms

Observed temperatures can be elevated by any of above heating sources. Similar to the results by Bradford et al. (2005), Requena-Torres et al. (2012) constrained the temperatures of the molecular clouds in the southwest lobe of the CND to  $T_{\text{kin}} = 200^{+300}_{-70}$  K for a low excitation component and  $T_{\text{kin}} = 500^{+100}_{-210}$  K for a high excitation one. Possible heating mechanisms are as follows:

**Shocks:** Bradford et al. (2005) stated that this high temperature cannot be explained by UV-photons because of the high extinction in the clump, and proposed shock heating. In addition to the gas heating, fast shock waves can sputter molecules off the dust surface (Schilke et al. 1997), which may dramatically change the chemical composition in the gas phase and in particular sputtering is known to increase the abundance of SiO (Martín-Pintado et al. 1997).

**X-rays:** A strong X-ray flux can affect the chemistry by ionizing and heating its surroundings creating an X-ray dominated region (XDR). The current value of unabsorbed X-ray flux from Sgr A\* in its quiescent state, i.e., not during a flare, is estimated to

be  $L \sim 2 \times 10^{33} \text{ erg s}^{-1}$  in 2–10 keV range (Baganoff et al 2003). There are other X-ray sources nearby (Degenaar et al. 2012), but those are either too weak or too far to affect the molecular cloud. An estimation of the X-ray ionization rate as a function of the intervening total hydrogen column density is presented in Section A.1 and its effect is discussed in Section 6. Past high X-ray luminosities caused by increased activity of the central black hole have been suggested in the literature (e.g., Revnivtsev et al. 2004; Koyama et al. 2007; Nobukawa et al. 2010; Terrier et al. 2010; Ponti et al. 2010; Capelli et al. 2012). Although higher X-ray fluxes could affect the chemistry, the flares causing them are likely of short duration, and may have a minimal effect on the chemistry given that the average flux is much lower.

**UV-photons:** The star clusters in the center of the CND provide a strong UV field that could affect the chemistry. Taking  $L_* = 1.1 \times 10^7 L_\odot$  and  $d = 1 - 3 \text{ pc}$ , the UV radiation field would be  $G_0 \sim 10^4 - 10^5$  Habing field units if we use the rough estimation described in Section A.2. This high radiation field can affect the chemistry via photo-dissociation or photo-ionization of molecules. On the other hand, the effect of UV-photon enhancement on the abundances of certain species can be suppressed for total hydrogen column densities  $> N_{\text{H}} \sim 10^{22} \text{ cm}^{-2}$ , i.e.,  $A_v \sim 5$  (see Section 5.1.4). Since the density of molecular clouds is expected to be high ( $n_{\text{H}} > 6 \times 10^4 \text{ cm}^{-3}$ ), the depth of the photon-dominated regions (PDRs), i.e., the interface between the ionized and the molecular regions, must be less than 0.06 pc wide. Interferometric data show that the source size of our target molecular cloud has a size of  $\sim 0.3 \text{ pc}$  (Christopher et al. 2005). Considering it to be a 0.3-pc diameter sphere illuminated from one direction, 27% of the material could be considered to be a PDR ( $A_v < 5$ ) when  $n_{\text{H}} = 6 \times 10^4 \text{ cm}^{-3}$ , and 9 % for  $n_{\text{H}} = 2 \times 10^5 \text{ cm}^{-3}$ . Therefore, PDRs may have some effect on the chemistry if the density is low, but the fraction of PDR is insignificant within the single-dish beam of our observations (from 0.5 to 1.1 pc) when the density is as high as what we derive from the LVG analysis for most of the species as described in a later section of this paper. The detailed discussion of the effects of a PDR is discussed separately in Section 5.1.4.

**Cosmic-rays:** An enhancement of the cosmic-ray ionization rate has been proposed as an alternative source of heating for the gas (e.g., Yusef-Zadeh et al. 2013b). Although cosmic rays are likely to be an additional heating source, its ionization rate must be extremely high  $\zeta > 10^{-13} \text{ s}^{-1}$  in order to achieve a high temperature of  $T_{\text{kin}} > 280 \text{ K}$  (see also Ao et al. 2013, for a comparison of different heating mechanisms). Cosmic-rays also provide direct ionization and dissociation. The electrons produced by the ionization can also produce UV-photons by exciting H<sub>2</sub> molecules to the Lyman and Werner bands (Prasad & Tarafdar 1983). Both X-rays and cosmic-rays can generate these secondary UV-photons; the effects of X-rays on the chemistry are similar to those of cosmic rays although X-rays heat the gas more efficiently than cosmic rays. Although high-energy  $\gamma$ -ray emission from the very center of the Galaxy provides strong evidence for cosmic rays (Chernyakova et al. 2011), it is hard to constrain the cosmic-ray ionization rates of molecules from the  $\gamma$ -ray observations. This is due to the strong dependence of cosmic-ray ionization rates on the lower energy term of the cosmic-ray spectrum (Padovani et al. 2009; Indriolo et al. 2009), which is not well-known. It has been claimed that in the Central Molecular Zone (CMZ), a region of  $\sim$  a few  $\times 100 \text{ pc}$  around Sgr A\*,  $\zeta$  is higher than in regular spiral-arm Galactic giant molecular clouds (GMCs), with  $\zeta \gtrsim 1 \times 10^{-15} \text{ s}^{-1}$  (Goto et al. 2008, 2013, 2014; Yusef-Zadeh et al. 2013b). Observations of high-energy

gamma rays show higher flux around the Sgr A\* (see above), and a model of gamma-ray emission by Chernyakova et al. (2011) shows that an injection of lower energy cosmic-rays  $10^4$  yrs ago best reproduces the observed spectrum.

## 2.2. Volume Densities

A large range of volume densities<sup>1</sup>,  $n_{\text{H}}$ , has been reported for the molecular gas in the CND. A large velocity gradient (LVG) analysis of multi- $J$  CO lines yields to  $n_{\text{H}} = (0.4 - 8) \times 10^5 \text{ cm}^{-3}$  (Bradford et al. 2005; Requena-Torres et al. 2012), lower values than those estimated from the HCN emission ( $n_{\text{H}} \gtrsim 10^7 \text{ cm}^{-3}$ , Montero-Castaño et al. 2009; Christopher et al. 2005). However, recent analysis of multi- $J$  HCN lines reduced the discrepancy with the densities derived from CO observations ( $n_{\text{H}} = (0.2 - 20) \times 10^6 \text{ cm}^{-3}$ , Smith & Wardle 2014; Mills et al. 2013) for most of the CND clumps because the above-mentioned previous studies needed to assume the kinetic temperature for their single-line analysis. An exception is a clump with a very high density of  $n_{\text{H}} = (0.6 - 8) \times 10^7 \text{ cm}^{-3}$  found by Mills et al. (2013) in the southwest lobe in which a vibrationally excited HCN line was observed.

## 3. Observations and LVG analysis

The observations were conducted with 3- and 2-mm receivers of the IRAM 30m telescope and the FLASH+ receiver of the APEX telescope. Detailed information on the data will be presented in Riquelme et al. (in preparation). The observed positions of our survey are shown in Figure 1. The survey position of the IRAM 30m telescope is at an offset  $\Delta\alpha = -30''$ ,  $\Delta\delta = -30''$  and this telescope has an FWHM of  $28''$  at 86 GHz and  $16''$  at 145 GHz. The APEX survey was taken with the FLASH+ receiver observing a position with an offset of  $\Delta\alpha = -20.1''$ ,  $\Delta\delta = -30.1''$  with a FWHM of  $22''$  at 262 GHz and  $12''$  at 516 GHz. All offsets are relative to the position of Sgr A\* (the absolute coordinates:  $\alpha_{J2000} = 17:45:39.99$ ,  $\delta_{J2000} = -29:00:26.6$ ). The maximum and minimum beam sizes are shown in solid lines (IRAM 30m) and in dotted lines (APEX - FLASH+) in Figure 1. The molecular transitions used in this analysis are listed in Table 1.

There are multiple velocity components along the same line of sight. Figure 2 shows a spectrum of HCN(5-4) as an example of those velocity components. The emission from positive velocities arises from M-0.02-0.07 (" $20 \text{ km s}^{-1}$  cloud") or M-0.13-0.08 (" $50 \text{ km s}^{-1}$  cloud"), which may be interacting with the CND. The emission at negative velocities is thought to come from the CND (Amo-Baladrón et al. 2011). Interferometric data (e.g., Christopher et al. 2005) show a few peaks in our beam, namely, clumps O, P, and Q in their notation, each centered at  $-108$ ,  $-73$ , and  $-38 \text{ km s}^{-1}$ . We select the velocity range for our study based on the spectra shown in Montero-Castaño et al. (2009). Clump Q is centered at around  $\sim -40 \text{ km s}^{-1}$ , and may be affected by self-absorption. Clump P is centered around  $-70 \text{ km s}^{-1}$  while Clump O is centered at around  $-110 \text{ km s}^{-1}$ . Since emission with the velocity  $v > -90 \text{ km s}^{-1}$  is likely to arise from all three clouds, we use the velocity cut from  $v = -90$  to  $-120 \text{ km s}^{-1}$  for our analysis to target only Clump O, located at the Galactic offset around  $\Delta\alpha = -20''$ ,  $\Delta\delta = -20''$ . Smaller beams in higher frequency observations of each telescope will only partially cover our target clump. Thus, we treated the line

intensities differently for lines above 100 GHz for IRAM observations and lines above 400 GHz for APEX observations. When there are more than 3 transitions observed in other frequency ranges for the species (CS, SO, and SiO), these lines are omitted from the analysis, otherwise we assumed large (50%) uncertainties.

Since our lower  $J$   $^{12}\text{CO}$  data may be affected by high optical depth, we also used the  $^{13}\text{CO}(3-2)$ ,  $\text{CO}(6-5)$  and  $\text{CO}(7-6)$  transition for the LVG analysis of CO. When using  $^{13}\text{CO}$ , an isotopic ratio of  $^{12}\text{C}/^{13}\text{C} = 25$  is assumed, following Requena-Torres et al. (2012). Data of CO (6-5) and (7-6) are taken from Requena-Torres et al. (2012) where they mapped the whole CND with the CHAMP+ receiver (Kasemann et al. 2006) at the APEX telescope. It is also expected that HCN is optically thick, and  $\text{H}^{13}\text{CN}$  lines are used in the LVG analysis assuming the same isotopic ratio.

With the obtained velocity-integrated intensities, we conduct an LVG analysis using the non-LTE radiative transfer code RADEX (van der Tak et al. 2007) covering the parameter ranges:  $n_{\text{H}} = 2 \times 10^2 - 2 \times 10^7 \text{ cm}^{-3}$ , column densities of species  $X$   $N(X) = 10^{11} - 10^{19} \text{ cm}^{-2}$ , and fixed kinetic temperatures of  $T_{\text{kin}} = 100, 300, \text{ and } 500 \text{ K}$ . The interferometric HCN (1-0) data show that the cloud of our interest has a size of  $0.33 \text{ pc}$  (Christopher et al. 2005), while a smaller source size of  $0.16 \text{ pc}$  is reported from mapping of higher- $J$  lines (Montero-Castaño et al. 2009). Thus, we run our analysis for different source sizes of  $0.1, 0.2, \text{ and } 0.3 \text{ pc}$ . Since our LVG analysis did not yield valid solutions for a source size  $< 0.3 \text{ pc}$ , we assume a source size of  $0.3 \text{ pc}$  for the results shown in the following sections. The brightness temperature was derived as  $T_b = T_{\text{MB}}\theta_s^2/(\theta_s^2 + \theta_b^2)$ , where  $T_{\text{MB}}$  is the measured main beam temperature,  $\theta_s$  is the source size, and  $\theta_b$  is the beam size of the telescope. The observed lines in the CND are listed in Table 1 while results from the LVG analysis are shown in Table 2. The derived values of column densities have little dependence on temperatures. Other than the listed species,  $\text{CH}_3\text{OH}$  and  $\text{C}_2\text{H}$  were also detected with strong intensities, but their lines were blended, making the LVG analysis very uncertain. These blended lines are omitted from the analysis. Since only one line of NO was detected, a temperature of  $T_{\text{kin}} = 300 \text{ K}$  and a density range of  $n_{\text{H}} = 2 \times 10^5 - 2 \times 10^6 \text{ cm}^{-3}$  are assumed for this molecule to obtain the range of column density. The column densities obtained from our LVG analysis at  $T_{\text{kin}} = 300 \text{ K}$  as well as the best-fit  $\text{H}_2$  densities are listed in Table 2. Due to the uncertainty in the high frequency observations mentioned above, volume densities for these species (CN,  $\text{H}_2\text{CO}$ ,  $\text{N}_2\text{H}^+$ , HCN,  $\text{HC}_3\text{N}$ , and  $\text{H}^{13}\text{CO}^+$ ) are very uncertain and therefore not shown.

## 4. Chemical Models

To model the chemistry of the observed molecular cloud in the CND we use the time-dependent gas-grain code, UCL\_CHEM (Viti et al. 2004), complemented with the parametric shock model of Jiménez-Serra et al. (2008). Gas-phase reactions in this model are taken from the Rate06 version of the UMIST database (Woodall et al. 2007). Details of the coupled code can be found in Viti et al. (2011). For our study we run the code in two phases. In Phase I, a diffuse cloud with an initial density of  $100 \text{ cm}^{-3}$  collapses to a core of chosen pre-shock densities. Models are run assuming that initially half of hydrogen is in atomic form while the other half in molecular form,  $\text{C}^+$ ,  $\text{S}^+$ ,  $\text{Mg}^+$ ,  $\text{Si}^+$  are in ionic form, and O, N, and He are in the atomic form. We assume free fall collapse and a cosmic ray ionization rate of  $\zeta = 10^{-17} \text{ s}^{-1}$  and a standard interstellar radiation field,  $G_0 = 1$ . The mod-

<sup>1</sup> In this paper, number densities are presented in terms of total hydrogen densities, which are common in theoretical papers instead of  $\text{H}_2$  densities, which are conventionally used in observational papers.

els are run for 3 different pre-shock densities,  $n_{\text{H}} = 2 \times 10^4$ ,  $2 \times 10^5$ , and  $2 \times 10^6 \text{ cm}^{-3}$ . In Phase II, the code is run for 4 shock velocities of  $v_s = 10, 20, 30$  and  $40 \text{ km s}^{-1}$  and the molecular abundances are followed along the propagation of the shock. We also run models with an increased cosmic-ray ionization rate but without shocks. Maximum temperatures and post-shock densities for corresponding velocities and densities are summarized in Table 3. Cosmic-ray ionization rates are varied from  $\zeta = 10^{-17}$  to  $10^{-13} \text{ s}^{-1}$ . In this paper, values of  $\zeta$  are expressed with respect to  $\text{H}_2$ , not H (i.e.,  $\zeta_{\text{H}_2}$ ). In Phase II,  $\zeta$  is enhanced at the same time as the shock waves pass.

The effect of sputtering is included by considering saturation time-scales for silicon, times for which the silicon abundance in the gas-phase changes by less than 10% between two time steps by sputtering (see Jiménez-Serra et al. 2008). Saturation time scales are also shown in Table 3 and temperatures and densities for  $n_{\text{H,pre}} = 2 \times 10^4 \text{ cm}^{-3}$  and  $n_{\text{H,pre}} = 2 \times 10^5 \text{ cm}^{-3}$  with shock velocities of  $v_s = 10, 20, 30$ , and  $40 \text{ km s}^{-1}$  are shown in Figure 3.

Sputtering by shock waves can vary the elemental abundances of the molecular clouds. For different shock velocities, different elemental abundances E1 and E2 are used (Table 4). When the shock velocities are smaller than  $20 \text{ km s}^{-1}$ , the elemental abundances of E1, "low-metal abundances", were applied. For higher shock velocity where the core sputtering of grains needs to be considered, E2 was used. This set of elemental abundances considers the depletion of metals onto the dust grains and is widely used for cold core chemical modeling as in Wakelam & Herbst (2008). Since ice mantles are sputtered by shocks only partially for  $v_s = 10 \text{ km s}^{-1}$ , only 10 % of the mantles are considered to be sputtered. For shock velocities  $v_s \geq 30 \text{ km s}^{-1}$ , sputtering from the core of dust grains starts to occur. Thus, the higher elemental abundances of E2 were used for shock velocities of  $v_s = 30$  and  $40 \text{ km s}^{-1}$  considering this core sputtering. The fraction of core sputtering of Si in E2 is taken from the results by Jiménez-Serra et al. (2008) for the degree of core sputtering caused by  $v_s = 30$  and  $40 \text{ km s}^{-1}$ . The value of Mg in E2 is estimated by assuming that 3 % of elemental Mg is sputtered from the grain core, which is a similar percentage as that of elemental Si. The sum of the elemental abundances for Mg and Fe was used for the Mg elemental abundance since the ionization of both Mg and Fe inject large amounts of free electrons which affects the chemistry, and this model currently does not contain Fe chemistry. The total elemental abundances of Si, Mg, and Fe abundances are taken from Anders & Grevesse (1989).

The treatment of Si core sputtering for  $v_s \geq 30 \text{ km s}^{-1}$  is only approximated in our model. Precise fractional abundances should be obtained with models such as those by Gusdorf et al. (2008); Jiménez-Serra et al. (2008); Flower & Pineau des Forêts (2012), especially for SiO. In addition, physical parameters such as the temperature and the density are parameterized in our model. For precise values of physical parameters, see Gusdorf et al. (2008); Flower & Pineau des Forêts (2012).

In order to study the effects of UV-photons, we use the publicly available Meudon PDR code *version 1.4.4* (Le Petit et al. 2006), which we run separately from the shock model code. This code calculates steady-state abundances without the time dependence. Since the chemistry can reach steady state at a very low  $A_V$  within about 100 years, results in low  $A_V$  should be reasonable.

## 5. Results of Chemical Modeling

### 5.1. Dependence on the Physical Conditions

As previously mentioned, chemical abundances are dependent on their pre-shock values, the physical structures of shock waves, cosmic-ray ionization rates, elemental abundances, densities, UV-photons, and their time evolution. In this subsection, we summarize the behavior of chemical abundances in the shock model with the variation of these parameters. First, the fractional abundances in pre-shock conditions are listed in Table 5 for each pre-shock density of  $n_{\text{H}} = 2 \times 10^4$ ,  $2 \times 10^5$ , and  $2 \times 10^6 \text{ cm}^{-3}$ , as a result of Phase I modeling. Since observed regions include different time steps of the shock passage, fractional abundances averaged over time are calculated. Plots of these time-averaged fractional abundances of observed species and  $\text{H}_2\text{O}$  in the post-shock phase (Phase II) are shown as examples in Figures 5 & 6 for  $n_{\text{H}} = 2 \times 10^5 \text{ cm}^{-3}$ ,  $v = 20 \text{ km s}^{-1}$ , and varying cosmic-ray ionization rates of  $\zeta = 1 \times 10^{-17} \text{ s}^{-1} - 1 \times 10^{-13} \text{ s}^{-1}$  to see the effects of cosmic-ray ionization. In order to demonstrate the effects of varying shock velocities, Figures 7 and 8 show post-shock time-averaged fractional abundances of observed species and  $\text{H}_2\text{O}$  for pre-shock densities of  $n_{\text{H}} = 2 \times 10^5 \text{ cm}^{-3}$ , a cosmic-ray ionization rate of  $\zeta = 1 \times 10^{-16} \text{ s}^{-1}$ , with varying shock velocities of 10, 20, 30, and  $40 \text{ km s}^{-1}$ . As shown in Table 3, higher shock velocities mean higher maximum temperatures. Abundance ratios of  $\text{H}_3\text{O}^+/\text{H}_2\text{O}$  and  $\text{HNC}/\text{HCN}$  are also shown in Figure 6 and 8, respectively.

#### 5.1.1. Pre-shock abundances

Molecules on the grain mantle are ejected after the shock waves pass, producing an increase of their gas-phase abundances in the post-shock phase. Significant amounts of some species such as HCN, HNC,  $\text{H}_2\text{CO}$  and NO are depleted on the grain surface before the shock passes (Table 5). For other species, even if the fractional abundances in the ice phase are not very high, their post-shock abundances in the gas phase can be increased from the ejection of other species. For example, ionic species (e.g.,  $\text{HCO}^+$  and  $\text{H}_3\text{O}^+$ ) are assumed to be neutralized when they are depleted on grains, but their abundances can be enhanced after shock when their neutral counterparts (e.g., CO and  $\text{H}_2\text{O}$ ) that have high abundances on ice mantles are released in the gas phase. Water, CO, and  $\text{N}_2$  have high fractional abundances on the ice ( $\sim 3 \times 10^{-5} - 1 \times 10^{-4}$ ,  $\sim 3 \times 10^{-7} - 4 \times 10^{-5}$ ,  $\sim 2 \times 10^{-7} - 6 \times 10^{-6}$ , respectively, with higher ice abundances for higher pre-shock densities), which enhance the abundances of their protonated species  $\text{H}_3\text{O}^+$ ,  $\text{HCO}^+$ , and  $\text{N}_2\text{H}^+$  after the shock passes. In addition, the fractional abundance of  $\text{H}_2\text{S}$  on the ice is very high since our model favors hydrogenation reactions on grains. Thus, the sputtering of  $\text{H}_2\text{S}$  ice also causes the increase of the fractional abundances of sulfur species such as CS and SO. Similarly, major Si-containing species on ice ( $\text{SiH}_4$  in our model) can react to form SiO after its ejection into the gas-phase (Schilke et al. 1997). It has been shown from the study of low-mass pre-stellar cores that the evaporation of  $\text{CH}_4$  can lead to the formation of carbon-chain molecules including  $\text{HC}_3\text{N}$  (Sakai et al. 2008). The pre-shock fractional abundance of  $\text{CH}_4$  on the grain surface is also high in this model, around  $10^{-5}$ . In this model, radicals such as CN are assumed to be hydrogenated immediately after they are depleted on grains, and their pre-shock abundances are not shown in the table.

### 5.1.2. Dependence of shock velocities

After the shock, the HCN fractional abundance can be further increased by the high temperature chemistry induced by the shock waves due to endothermic reactions that convert HNC and CN to HCN (Figure 8). The following reaction involving CN



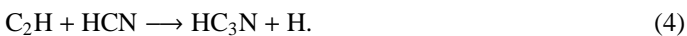
has a reaction barrier of 820 K. When the temperature becomes high enough for the collisional dissociation of molecular hydrogen to occur ( $\sim 4000$  K) via reaction of the form  $\text{H}_2 + \text{M} \longrightarrow \text{H} + \text{H} + \text{M}$  where M is any given species (most often  $\text{H}_2$  or H), 90 % of hydrogen is rapidly converted into the atomic form. Such collisional dissociation occurs in our model when  $n_{\text{H}} \geq 2 \times 10^5 \text{ cm}^{-3}$  and  $v_s = 40 \text{ km s}^{-1}$ . Then, the reverse reaction of the reaction (1) becomes more important, increasing the CN abundance. The fractional abundance of HNC decreases by the reaction:



The rate coefficient of this reaction has a strong temperature dependence<sup>2</sup> ( $k \propto T^{4.5}$ ), and the ratio HCN/HNC increases when the maximum temperature caused by the shock waves is higher, and the abundance ratio of HCN/HNC  $> 10$  is reached for the model  $v_s > 30 \text{ km s}^{-1}$  for all densities in our models (see Figure 8). Abundances of ionic species decrease after the shock because metal species such as Mg are sputtered into the gas-phase and become atomic ions, taking over the positive charge from molecular ions. Therefore, the case of  $v_s = 10 \text{ km s}^{-1}$  with less sputtering has a higher  $\text{HCO}^+$  and  $\text{N}_2\text{H}^+$  abundance. As for  $\text{H}_3\text{O}^+$ , which has higher proton affinity than  $\text{HCO}^+$  and  $\text{N}_2\text{H}^+$ , the fractional abundance after the shock decreases less than that of these species. When  $v_s = 40 \text{ km s}^{-1}$ , the ionization fraction increases and the fractional abundances of  $\text{HCO}^+$ ,  $\text{N}_2\text{H}^+$ , and  $\text{H}_3\text{O}^+$  increase. Since a high abundance of sulfur is sputtered from grains, the CS and SO fractional abundances increase after the shock especially for  $v_s > 30 \text{ km s}^{-1}$ . The increase of a fractional abundance due to the sputtering is even more noticeable in the case of SiO. As mentioned in Section 4, the amount of the core elements sputtered from shock waves with  $v_s > 30 \text{ km s}^{-1}$  is a rough estimate in this model, and a more careful treatment should be used for a better prediction of SiO's fractional abundances. The fractional abundances of NO increase slowly after the shock passes because the evaporation of  $\text{NH}_3$  can initiate the reaction:



where NH is produced through the dissociation of  $\text{NH}_3$ . There is no strong dependence on the shock velocity except for the case of  $v_s = 40 \text{ km s}^{-1}$  for NO. The fractional abundance of  $\text{H}_2\text{CO}$  does not strongly depend on shock velocities. The only difference is that for increasing  $v_s$ ,  $\text{H}_2\text{CO}$  is injected into the gas phase at earlier times due to the shorter saturation times. The fractional abundance of  $\text{HC}_3\text{N}$  for  $v_s \leq 30 \text{ km s}^{-1}$  only increases after  $10^4$  yrs while the increase happens earlier for  $v_s = 40 \text{ km s}^{-1}$ , around 1000 yrs or so. Higher maximum temperatures,  $T_{\text{max}}$ , caused for higher shock velocities increase the  $\text{HC}_3\text{N}$  fractional abundances since they accelerate some endothermic reactions such as



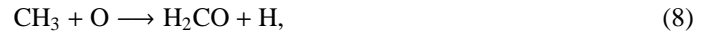
<sup>2</sup> The temperature dependence of the rate coefficient of this reaction is derived by fitting experimental values. A temperature dependence that has a physical meaning should be in the form of  $\exp(-\gamma/T)$  where  $\gamma$  is a reaction barrier (see Graninger et al. 2014, for detailed analysis of HNC/HCN ratio).

### 5.1.3. Dependence on cosmic-ray ionization rate

In the models we run, the increase in  $\zeta$  in Phase II causes the peak value of the HCN abundance ( $\sim 3 - 10 \times 10^{-7}$ ) to occur earlier in time. However, a high  $\zeta$  also decreases the fractional abundance of HCN faster in the post-shock region than low values of  $\zeta$ . Regarding the dependence on the cosmic-ray ionization rate, HNC has a similar behavior to HCN; a higher cosmic-ray ionization rate helps the formation of HNC on a shorter time scale. This trend by the higher cosmic-ray ionization rate to shorten the chemistry time scale also applies to other species such as CS, SO, SiO, NO, and  $\text{HC}_3\text{N}$ . Although varying  $\zeta$  does not change the peak value itself, it shortens the time span in which the higher fractional abundances are attained. While the HCN/HNC ratio has some temperature dependence, it decreases with higher cosmic-ray ionization rate because a high ionization fraction makes the  $\text{HCNH}^+$  abundance high and a following reaction brings the HCN/HNC ratio closer to unity:



whose branching ratios are 34%, 34%, and 33%, respectively. Although CN is an unstable radical, a high ionization fraction caused by a high cosmic-ray ionization rate can keep the CN fractional abundance high via reaction (7) above. A higher cosmic-ray ionization rate also increases the abundances of ionic species such as  $\text{N}_2\text{H}^+$ ,  $\text{HCO}^+$ , and  $\text{H}_3\text{O}^+$ . The proton affinity of  $\text{H}_2\text{O}$  is higher than those of CO and  $\text{N}_2$ , and CO has a higher value than  $\text{N}_2$ . This means that CO is more likely to be protonated than  $\text{N}_2$ , and a reaction such as  $\text{N}_2\text{H}^+ + \text{CO} \longrightarrow \text{N}_2 + \text{HCO}^+$  is much faster than its reverse reaction. The fractional abundance of a protonated species of a lower proton affinity such as  $\text{N}_2\text{H}^+$  has a stronger dependence on the cosmic-ray ionization rate. The increase of a peak fractional abundance of  $\text{H}_2\text{CO}$  at a higher cosmic-ray ionization rate is caused by the dissociation of  $\text{CH}_3\text{OH}$  via the gas-phase reactions



and the cosmic-ray-photodissociation reaction



### 5.1.4. Dependence on UV-field strength

Results obtained with the Meudon code (Le Petit et al. 2006) show that the fractional abundance of  $\text{HCO}^+$  and  $\text{H}_3\text{O}^+$  can be enhanced up to  $10^{-8}$  for  $A_V < 1$  when  $G_0 = 10^4$  Habing field units and  $n_{\text{H}} = 2 \times 10^5 \text{ cm}^{-3}$  (Figure 9). The peak value of CN is achieved at a larger value than those of  $\text{HCO}^+$  and  $\text{H}_3\text{O}^+$ , at  $A_V \sim 3$ . Unlike  $\text{HCO}^+$  and  $\text{H}_3\text{O}^+$ , the fractional abundance of  $\text{N}_2\text{H}^+$  is not enhanced in the low  $A_V$  regime (Figure 9). For other species, there is no enhancement in their fractional abundances in  $A_V < 1$  regions.

## 5.2. Comparison with Observations

We compare the observed column densities with the predictions of our chemical models in this section. Since chemical models give us fractional abundances, we opt for comparing ratios of column densities with ratios of fractional abundances (and hence make the implicit assumption that all molecules arise from the

same gas component). All our ratios are with respect to CO. The results of chemical modeling with different physical conditions mentioned in Section 4 are compared following the method used in Garrod et al. (2007). A confidence level for each species  $i$  is defined by

$$\kappa_i = \text{erfc} \left( \frac{|\log(X_{i,\text{calc}}) - \log(X_{i,\text{obs}})|}{\sqrt{2}\sigma} \right) \quad (10)$$

where  $\text{erfc}$  is a complementary error function in a form  $\text{erfc}(x) = \frac{2}{\sqrt{\pi}} \int_x^\infty e^{-t^2} dt$ ,  $X_{i,\text{calc}}$ ,  $X_{i,\text{obs}}$  are fractional abundances with respect to CO for molecules  $i$  predicted from models and observations respectively, and in the above formula, a value of  $\sigma = 1$  is used. The degree of agreement between model predicted and observed abundances is measured by an average value of  $\kappa_i$ ,  $\bar{\kappa}$ , for all the observed species. A value of  $\bar{\kappa} = 1$  means a perfect match, and  $\bar{\kappa} = 0.317$  means an average discrepancy of one order of magnitude. Since our calculation for SiO is only an approximation, values of  $\kappa$  are calculated for cases with and without SiO included. We found that there is no significant differences between the cases with and without SiO.

The maximum values of confidence level in each model over the post shock time of  $t = 0 - 10^5$  yrs are plotted in Figure 10. Models in a reasonable agreement ( $\kappa > 0.7$ ) with the observed abundances can be summarized in the following three categories: 1) low density models ( $n_{\text{H}} = 2 \times 10^4 \text{ cm}^{-3}$ ,  $v_s > 30 \text{ km s}^{-1}$ ,  $\zeta < 10^{-13} \text{ s}^{-1}$ ), 2) high velocity shock models ( $n_{\text{H}} = 2 \times 10^5 \text{ cm}^{-3}$ ,  $v_s = 40 \text{ km s}^{-1}$ ), and 3) high cosmic-ray ionization models ( $n_{\text{H}} = 2 \times 10^5 \text{ cm}^{-3}$ ,  $\zeta > 10^{-15} \text{ s}^{-1}$ ). In case 1), the chemistry is still in an early phase because a significant amount of atomic carbon is present, and because the radical and ionic species are abundant, resulting in a good agreement with the observed chemical features. In case 2), the maximum temperature is so high that the shock becomes dissociative, which means that the majority of molecular hydrogen is destroyed by collisions with molecular or atomic hydrogen. Over the short time period during which atomic hydrogen is abundant, the abundances of radical and ionic species increase. In case 3), the high cosmic-ray ionization rate keeps the abundances of radical and ionic species high. Example plots of fractional abundances and confidence levels are shown in Figures 11 for case 1), Figure 12 for case 2), and Figure 13 for case 3). For the cases without shocks, the agreement with the observations is better for the high cosmic-ray ionization rates, achieving a similar degree of agreement to models with shocks. The plausibility of each scenario is discussed in the next section.

## 6. Discussion

Although there are several different models that show a modest degree of agreement with observations, these cases can be constrained using other information.

### 6.1. Gas density

Our derived total hydrogen densities for the species we observed range from  $n_{\text{H}} = 2 \times 10^4 - 1.2 \times 10^6 \text{ cm}^{-3}$ . Mills et al. (2013) derived  $n(\text{H}) = 3 \times 10^7 \text{ cm}^{-3}$  from multi- $J$  observations of HCN for similar velocity range when including the high-lying  $J = 8 - 7$  transition. Smith & Wardle (2014) derived a total hydrogen density of  $2.6 \times 10^6 \text{ cm}^{-3}$  also from HCN lines although they used the entire velocity component around  $-80 \text{ km s}^{-1}$  instead of the velocity slice that we have used. The density derived from our observations of HCN are  $n_{\text{H}} = (6.94 - 10.5) \times 10^5 \text{ cm}^{-3}$

assuming  $T_{\text{kin}} = 300 \text{ K}$ , and for the case of  $T_{\text{kin}} = 100 \text{ K}$ ,  $n_{\text{H}} = (1.40 - 2.20) \times 10^6 \text{ cm}^{-3}$ . Since the temperatures used by Mills et al. (2013) and Smith & Wardle (2014) are 61 and 150 K respectively, our derived densities are roughly consistent considering the degeneracy between the derived density and the temperature. For the CO lines, the best-fit density in our analysis is  $1 \times 10^4 \text{ cm}^{-3}$ , which is similar to the value derived from multi- $J$  CO lines by Requena-Torres et al. (2012) and Bradford et al. (2005). Since we used the high- $J$  CO line data from Requena-Torres et al. (2012), this similarity is expected. The derived densities of other molecules are  $n_{\text{H}} > 2 \times 10^5 \text{ cm}^{-3}$  except for  $\text{H}_3\text{O}^+$ . For the case of  $\text{H}_3\text{O}^+$ , the density is derived from two lines whose energy levels are close together, and the solution has a large uncertainty. If we use the density of other species ( $n_{\text{H}} > 2 \times 10^5 \text{ cm}^{-3}$ ), the low-density scenario of  $n_{\text{H}} \sim 2 \times 10^4 \text{ cm}^{-3}$  in Section 5.2 is excluded.

The tidal stability of the core in the CND is determined by the following equation (Christopher et al. 2005)

$$n(\text{H}_2) = 2.87 \times 10^7 \left[ \left( \frac{R}{\text{pc}} \right)^{-3} + 0.4 \left( \frac{R}{\text{pc}} \right)^{-1.75} \right] \text{ cm}^{-3} \quad (11)$$

where  $R$  is a Galactocentric radius. The core becomes tidally unstable when  $n_{\text{H}} < 2.8 \times 10^7 \text{ cm}^{-3}$  for  $R = 1.5 \text{ pc}$  and when  $n_{\text{H}} < 1.4 \times 10^7 \text{ cm}^{-3}$  for  $R = 2 \text{ pc}$ . Densities derived by our analysis are still lower than this limit even for HCN with the large dipole moment whose lines have higher critical densities. This result suggests that the core is tidally unstable. On the other hand, Mills et al. (2013) found a clump that may be gravitationally stable in their observation of the HCN emissions in the CND. Their use of higher transition lines ( $J = 9 - 8$  and a vibrationally excited line) may have resulted in their tracing a higher excitation or higher density portion, while we are tracing the bulk material of the clump. Since Mills et al. (2013) concluded that the bulk of the gas except for one clump is tenuous and gravitationally unstable, our results are overall consistent with theirs.

### 6.2. High velocity shocks

It has been shown in Figure 10 that a high shock velocity case ( $v_s = 40 \text{ km s}^{-1}$ ) apparently gives a good agreement with the observations. However, the time span required for attaining an agreement is very short ( $t \sim 3 \times 10^2$  yrs) as shown in Figure 12. In this time span, the temperature should still be over 1000 K, which is not supported by previous studies found in the literature. However, if such high velocity shocks are occurring in short periods of time, that may also give a good agreement with the observations. Requena-Torres et al. (2006) suggested shocks in the Galactic Center as  $5 \times 10^4$  yrs although this time scale is much longer than the time suggested by our high velocity shock case.

### 6.3. Cosmic-ray dominated gas

If we assume a density  $\gtrsim$  a few  $\times 10^5 \text{ cm}^{-3}$  as our results of the LVG analysis for most species show, models with a higher cosmic-ray ionization rate of  $\zeta > 10^{-15} \text{ s}^{-1}$  show the best agreement with the observed column densities. This is in agreement with previous studies in other parts of the Galactic Center region (e.g., Yusef-Zadeh et al. 2013a). The level of agreement stays high until  $t \sim 10^3 - 10^4$  yrs after the passage of the shock wave. The derived cosmic-ray ionization rate is about 2-4 orders of magnitude higher than the regular value in dense molecular

clouds in the spiral arms of  $(1 - 5) \times 10^{-17} \text{ s}^{-1}$ . A high cosmic-ray ionization rate in the CND is not very surprising since analysis of high-energy  $\gamma$ -ray emission in the Galactic Center claimed that most of this  $\gamma$ -ray emission comes from within 3 pc from Sgr A\* (Linden et al. 2012). Some previous studies have also claimed high values for the cosmic-ray ionization rate in the Galactic Center. For example, Goto et al. (2013, 2014) studied the cosmic-ray ionization rate in the CND. In their earlier work, they derived  $\zeta \sim 1.2 \times 10^{-15} \text{ s}^{-1}$  from their  $\text{H}_3^+$  observations while  $\gamma$ -ray observations indicate 4 orders of magnitude higher values. In their more recent work, they claimed that  $\zeta$  is well above  $10^{-15} \text{ s}^{-1}$  (Goto et al. 2014). For a cosmic-ray ionization rate of  $\zeta > 10^{-12} \text{ s}^{-1}$ , as suggested by  $\gamma$ -ray observations, the molecules start to dissociate in a short time scale ( $\sim 10^3$  yrs). Since cosmic rays have high penetration depth, an enhancement of the cosmic-ray ionization rate as in the CND should also appear in other locations in the Galactic Center. This is consistent with other studies such as that by van der Tak et al. (2006) who claimed higher cosmic-ray ionization rate of  $\zeta = 4 \times 10^{-16} \text{ s}^{-1}$  in Sgr B2 as well as the work of Yusef-Zadeh et al. (2007), who claimed  $\zeta = 5 \times 10^{-13} \text{ s}^{-1}$  ( $\zeta_H = 0.5\zeta_{H_2}$ ) on average in Sgr B1, Sgr B2, Sgr C, Radio Arc and Arches Cluster.

We note our LVG analysis gives different volume densities for CO than for any other species. In fact it is possible that CO is tracing a larger gradient in density than any other species analysed in this study because its emission may come from extended regions. Although the high- $J$  transitions of CO used in our analysis is likely to trace relatively compact and dense regions as other species, the uncertainty of the derived CO column density needs to be investigated. To test how sensitive our results would be to variations in CO column densities, we have calculated the confidence level for CO column densities a factor of 3 higher and lower than what we derived. We find that when a higher CO column density is used, the best fit cosmic-ray ionization rate is lower by approximately one order of magnitude, while the opposite is true when a lower CO column density is used. Since it is likely that the CO emission is extended, the real CO column density in the region traced by the other molecules will be lower. Hence the upper value of our best fit cosmic ray ionization rate is in fact conservative and our conclusion that the gas chemistry is dominated by cosmic rays is still valid. Of course, our results should be confirmed with higher angular resolution observations of the CMZ.

#### 6.4. Effects of UV-photons

Depending on the geometry of the molecular cloud, the surface area exposed to the central star cluster might be large, which means that the molecular mass affected by UV photons might be significant. In that case, species such as CN and  $\text{HCO}^+$  become more abundant. These species are enhanced for higher cosmic-ray ionization rates as well. In addition, other factors to be considered are the beam size and the uncertainty of the source size that we used. The largest beam size is  $28''$ , which might include emission from more tenuous and extended parts of the CND. Those parts are more likely to be influenced by UV-photons, which may increase the abundance of  $\text{HCO}^+$  and CN. Increase of these radicals and ions by UV-photons may misleadingly give a good agreement of observations with a higher cosmic-ray ionization rate than the actual value. Since cosmic-rays can penetrate into larger column densities than UV-photons, higher resolution map of these species as well as that of  $\text{N}_2\text{H}^+$ , which is not abundant in PDRs, can help differentiating between the two scenarios. Furthermore, the enhancement of the cosmic-ray ionization rate

should affect larger regions in the CMZ than the UV-photons, and comparison with other positions in our survey can also help constraining the value of cosmic-ray ionization rate.

#### 6.5. Cosmic-rays or X-rays?

Our models do not include X-rays, but their effect on the chemistry is very similar to that of cosmic-rays, and variation of the X-ray ionization rate can be mimicked by that of the cosmic-ray ionization rate. The difference in penetration depth may help differentiating between the effect of X-rays and cosmic-rays. As shown in Figure 4, the X-ray ionization rate goes down below  $\zeta_X = 10^{-16} \text{ s}^{-1}$  quickly after the shielding column density of  $N_H = 10^{21} \text{ cm}^{-2}$  since we use a soft X-ray spectrum assuming most of the emission comes from stellar components as in Goto et al. (2013). Majority of the ionization is caused by these soft components. If the density is  $> 10^5 \text{ cm}^{-3}$ , this column density corresponds to 0.003pc, which is 1% of the size of the molecular cloud in length. Although the observed chemical composition agrees with the models with ionization rate  $\zeta > 10^{-15} \text{ s}^{-1}$ , X-rays are not likely the source of ionization if the average X-ray flux is similar to the value observed currently from Sgr A\*. As mentioned in Section 2, the X-ray activity may have been higher in the past. Although this higher (and harder spectrum) X-ray flux may have increased the X-ray ionization rate, the hard spectrum coming from the AGN may not significantly affect the ionization rate because of the smaller cross section. Also, the flares may be too short-lived to cause significant change in chemistry.

#### 6.6. Possibility of no shock

As stated in Section 5.2, models without shocks yield good agreement with observations if the cosmic-ray ionization rate is high. This is due to the desorption of ice induced by cosmic rays described in Roberts et al. (2007), and it can increase gas-phase abundances of shock-related molecules such as SiO. However, this mechanism of cosmic-ray induced photo-desorption has a large uncertainty in parameters. In addition, observations of ubiquitous complex organic molecules in the Galactic Center (Requena-Torres et al. 2008) indicates that shock waves are common in the Galactic Center. Therefore, it is very likely that shocks are present in the CND.

#### 6.7. Other factors

The models discussed in this paper assume an enhancement of the cosmic-ray ionization rate and the contemporaneous passage of a shock wave. There are of course other possibilities. The shock wave may have passed earlier/later than the enhancement of the cosmic-ray ionization rate. There might have been multiple shock waves in the past  $10^4$  yrs or so. The frequency of shock waves should be considered in future work with the help of hydrodynamic models of the CND. The pre-shock conditions have also some uncertainties. In our models, we run the pre-shock conditions with  $\zeta = 1 \times 10^{-17} \text{ s}^{-1}$  and  $G_0 = 1$ . It is likely that the enhancement of UV-field and cosmic-ray ionization rate has occurred before the shock passage, although it is almost impossible to trace the exact time evolution of these quantities.

The effects of turbulence may also need to be considered; it is possible that ionized or atomic gas might be fed into the molecular region continuously due to turbulence. The ionized gas may induce the chemical reactions similar to those in regions of high

X-ray/cosmic-ray ionization rate. The effect of turbulence needs to be further investigated.

## 7. Summary

We have analysed the line survey data taken with the IRAM 30-meter telescope and the 12-meter APEX telescope toward a position in the southwestern lobe of the circumnuclear disk of the Galactic Center. Using an LVG radiative transfer code to predict the emission from 15 different molecular species we have derived column densities and  $\text{H}_2$  volume densities implied by their excitation. A combined analysis of the excitation and the chemical modeling suggests that models with lower density ( $n_{\text{H}} \sim 2 \times 10^4 \text{ cm}^{-3}$ ), higher cosmic-ray ionization rate ( $\zeta > 10^{-15} \text{ s}^{-1}$ ), or high-velocity shocks ( $v_s > 40 \text{ km s}^{-1}$ ) give good agreement with the observations. Considering the density derived from our observations and the estimated temperature in previous studies, the scenario of high cosmic-ray ionization rate is favored, but chemical compositions can also be partially affected by UV-photons or X-rays if the structure of the cloud is clumpy or filamentary. Future study is needed both in terms of modeling and observation. Since the source is very heterogeneous, one-dimensional model that include XDRs and PDRs may be necessary. Observationally, high spatial resolution interferometric maps that resolve the different structures are essential for the interpretation of this complex source. ALMA observations of the CND by Mills et al. (in preparation) should reveal such morphology of physical conditions in the CND.

comes  $1.1 \times 10^7 L_{\odot}$ . Using Equation (9.1) in Tielens (2005), the radiation field strength  $G_0$  becomes

$$G_0 = 625 \frac{L_* \chi}{4\pi d^2} = 1.3 \times 10^5 (\chi/1)(d/1\text{pc})^{-2}, \quad (\text{A.2})$$

where  $L_*$  is the luminosity of the star,  $\chi$  is the fraction of luminosity above 6 eV, and  $d$  is the distance from the star.

## Appendix A: Estimation of Physical Conditions

### A.1. X-ray ionization rate

As for the calculation of X-ray ionization rate, we followed the procedure described in Goto et al. (2013). From the X-ray luminosity measured in the 2-10 keV range by Baganoff et al. (2003)  $L_X = 2 \times 10^{33} \text{ erg s}^{-1}$ , X-ray flux in 0.1-2 keV range was estimated from the ATOMDB program (Foster et al. 2012) with the plasma temperature of 1.9 keV. The ionization rate was taken to be

$$\zeta_X = \int \sigma_{\text{tot}}(E) \frac{E}{W(1\text{keV})} F(E) dE, \quad (\text{A.1})$$

where  $\sigma_{\text{tot}}(E)$  is the ionizing cross section including the photo-ionization from heavy elements and Compton scattering at energy  $E$ ,  $W$  is the mean energy required for ionization (Dalgarno et al. 1999), and  $F(E)$  is the flux at energy  $E$ . For  $W$ , a value at  $E = 1 \text{ keV}$  was used. In addition to the calculation by Goto et al. (2013), we calculated the dependence of X-ray ionization rate on the shielding hydrogen column densities  $N$ . The flux at energy  $E$  becomes  $F(E, N) = F_0 \exp(-\sigma_{\text{tot}}(E)N)$ . We also used 2 pc as the distance to the source. The calculated X-ray ionization rate is shown in Figure 4.

### A.2. UV-photon flux

Lacy et al. (1980) estimated the number of ionizing photon flux to be  $2 \times 10^{50} \text{ s}^{-1}$  with the effective temperature of  $T_{\text{eff}} = 31,000 - 35,000 \text{ K}$ . From the stellar parameters listed in Tielens (2005), we consider spectral types of the stars in the central cluster to be similar to B0 types. The total number of ionizing photons is translated into  $\sim 140$  stars, and the total luminosity be-



Molecule	Transition	Freq. (GHz)	$\int_{-120}^{-90} T_{MB} dv$ (K km s <sup>-1</sup> )
CO	4-3	461.04	501.83
	6-5	691.47	895.68
	7-6	806.65	877.8
HCN	1-0	88.632	56.860
	4-3	354.51	89.725
	5-4	443.116	88.629
HNC	1-0	90.664	8.0164
	3-2	271.981	10.561
	4-3	362.630	8.5620
HCO <sup>+</sup>	1-0	89.1885	23.681
	4-3	356.7343	45.648
SiO	2-1	86.847	2.0543
	8-7	347.331	1.8295
	9-8	390.729	1.7224
CS	2-1	97.981	12.130
	6-5	293.912	22.196
	7-6	342.883	22.423
	8-7	391.847	22.484
p-H <sub>2</sub> CO	2 <sub>0,2</sub> - 1 <sub>0,1</sub>	145.603	2.1535
	4 <sub>0,4</sub> - 3 <sub>0,3</sub>	290.623	0.95264
N <sub>2</sub> H <sup>+</sup>	3-2	279.512	1.6709
	4-3	372.673	1.7412
	5-4	465.825	1.2520
SO	2 <sub>3</sub> - 1 <sub>2</sub>	99.300	1.0909
	7 <sub>8</sub> - 6 <sub>7</sub>	304.077	3.7813
	8 <sub>9</sub> - 7 <sub>8</sub>	346.527	3.7220
	9 <sub>10</sub> - 8 <sub>9</sub>	389.120	3.9306
CN	1 <sub>1/2</sub> - 0 <sub>1/2</sub>	113.169	14.283
	1 <sub>3/2</sub> - 0 <sub>1/2</sub>	113.495	14.004
	3 <sub>7/2</sub> - 2 <sub>5/2</sub>	340.249	29.820
HC <sub>3</sub> N	10-9	90.979	0.54742
	18-17	163.753	1.0548
NO	4-3	350.69	2.4023
p-H <sub>3</sub> O <sup>+</sup>	3 <sub>2</sub> + -2 <sub>2</sub> -	364.797	2.5981
	3 <sub>1</sub> + -2 <sub>1</sub> -	388.459	2.1160
<sup>13</sup> CO	3-2	330.588	25.334
H <sup>13</sup> CN	1-0	86.3399	5.0428
	2-1	172.6778	10.346
	4-3	345.3398	9.0259
	1-0	86.7543	1.1076
H <sup>13</sup> CO <sup>+</sup>	2-1	173.5067	1.4072
	4-3	346.9983	1.3180

**Table 1.** A list of spectral lines used for chemical analysis. Their transitions, frequencies, and velocity-integrated intensities in the range of -120 to -90 km s<sup>-1</sup> are shown.

Species	Column Densities (cm <sup>-2</sup> )	Hydrogen Densities (cm <sup>-3</sup> )
CS	$(1.07 \pm 0.13) \times 10^{15}$	$(7.26 \pm 1.18) \times 10^5$
CN	$(5.48 \pm 3.75) \times 10^{15}$	—
H <sub>2</sub> CO	$(5.01 \pm 2.76) \times 10^{13}$	—
SO	$(4.46 \pm 0.61) \times 10^{14}$	$(1.10 \pm 0.21) \times 10^6$
N <sub>2</sub> H <sup>+</sup>	$(1.47 \pm 0.58) \times 10^{13}$	—
H <sub>3</sub> O <sup>+</sup>	$(9.44 \pm 0.38) \times 10^{14}$	$(7.18 \pm 3.32) \times 10^4$
SiO	$(7.95 \pm 0.49) \times 10^{13}$	$(5.04 \pm 0.32) \times 10^5$
HCN	$(3.38 \pm 0.40) \times 10^{15}$	$(8.70 \pm 1.76) \times 10^5$
HCO <sup>+</sup>	$(5.26 \pm 1.28) \times 10^{14}$	$(2.34 \pm 0.84) \times 10^5$
HNC	$(1.90 \pm 0.29) \times 10^{14}$	$(5.46 \pm 0.88) \times 10^5$
HC <sub>3</sub> N	$(2.87 \pm 0.58) \times 10^{13}$	—
NO	$(3.02 \pm 0.61) \times 10^{15}$	—
CO	$(2.23 \pm 0.35) \times 10^{18}$	$(2.28 \pm 0.52) \times 10^4$
H <sup>13</sup> CN	$(9.70 \pm 2.30) \times 10^{13}$	$(4.44 \pm 2.00) \times 10^5$
H <sup>13</sup> CO <sup>+</sup>	$(4.02 \pm 2.55) \times 10^{13}$	—

**Table 2.** A list of best-fit column densities and number densities derived from the LVG analysis. Densities for some species are not shown due to the larger uncertainty considered as a consequence of the partial source coverage by the beam (see Section 3). Because CO and HCN are likely to be optically thick, <sup>13</sup>C isotopologues are also used in the LVG analysis assuming the <sup>12</sup>C/<sup>13</sup>C ratio of 25.

$n_{\text{H,pre}}(\text{cm}^{-3})$	$n_{\text{H,post}}(\text{cm}^{-3})$	$v_s$ (km/s)	$T_{\text{max}}$ (K)	$t_{\text{sat}}$ (yr)
$2 \times 10^4$	$6.1 \times 10^4$	10	300	95.4
$2 \times 10^4$	$1.0 \times 10^5$	20	900	57.0
$2 \times 10^4$	$1.3 \times 10^5$	30	1800	44.0
$2 \times 10^4$	$1.6 \times 10^5$	40	2200	45.5
$2 \times 10^5$	$6.3 \times 10^5$	10	300	10.5
$2 \times 10^5$	$1.0 \times 10^6$	20	800	5.7
$2 \times 10^5$	$1.4 \times 10^6$	30	2000	4.4
$2 \times 10^5$	$1.7 \times 10^6$	40	4000	4.6
$2 \times 10^6$	$6.3 \times 10^6$	10	300	1.0
$2 \times 10^6$	$1.0 \times 10^7$	20	800	0.6
$2 \times 10^6$	$1.4 \times 10^7$	30	2000	0.4
$2 \times 10^6$	$1.7 \times 10^7$	40	4000	0.5

**Table 3.** Shock velocities used in this model and corresponding saturation times and maximum temperatures taken from Jiménez-Serra et al. (2008). In their paper,  $t_{\text{sat}}$  is defined as the time when sputtering of dust grains "saturates" the silicon abundance (i.e., when the silicon abundance changes between two consecutive time steps by less than 10 %). Symbols  $n_{\text{pre}}$  and  $n_{\text{post}}$  stand for pre-shock and post-shock densities, respectively.

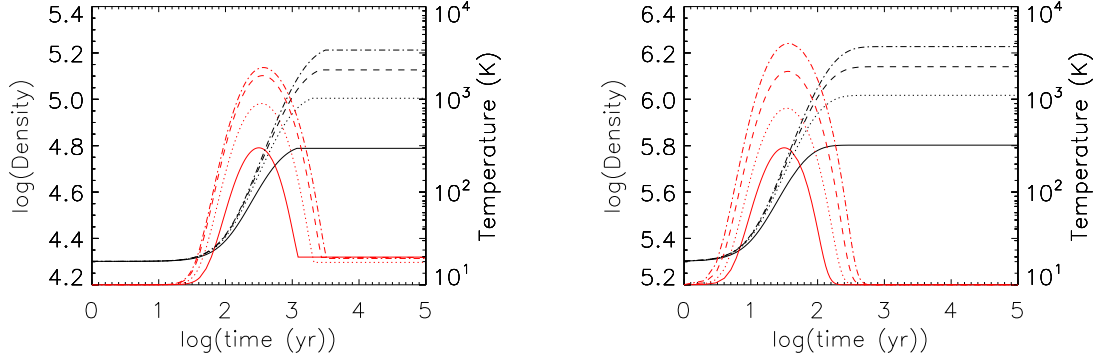


**Fig. 3.** The temperatures (red lines with the scale on the right ordinate) and densities (black lines with the scale on the left ordinate) after the shock are shown for  $n_H = 2 \times 10^4 \text{ cm}^{-3}$  (left panel) and  $n_H = 2 \times 10^5 \text{ cm}^{-3}$  (right panel) with varying shock velocities of  $v_s = 10, 20, 30$ , and  $40 \text{ km s}^{-1}$ . Different velocities are indicated with solid lines ( $10 \text{ km s}^{-1}$ ), dotted lines ( $20 \text{ km s}^{-1}$ ), dashed lines ( $30 \text{ km s}^{-1}$ ), and dash-dotted lines ( $40 \text{ km s}^{-1}$ ).

Element	E1	E2
He	0.14	0.14
C	$7.3\text{e-}5$	$7.3\text{e-}5$
N	$2.1\text{e-}5$	$2.1\text{e-}5$
O	$1.8\text{e-}4$	$1.8\text{e-}4$
S	$8.0\text{e-}8$	$4.5\text{e-}7$
Si	$8.0\text{e-}9$	$1.0\text{e-}6$
Mg	$7.0\text{e-}9$	$2.4\text{e-}6$

**Table 4.** Elemental abundances used in the models with respect to the total hydrogen abundances. E1 is taken from the low-metal abundance case adopted in Wakelam & Herbst (2008) and taken from Graedel et al. (1982) and Morton (1974). For selected elements in E1, Si and Mg, we considered 3 % of sputtering from the abundances in Anders & Grevesse (1989), and other elements are taken from EA2 and EA3 of Wakelam & Herbst (2008).

Species	Pre-shock densities ( $\text{cm}^{-3}$ )		
	$2 \times 10^4$	$2 \times 10^5$	$2 \times 10^6$
HCN	3.6(-9)	2.8(-8)	6.1(-10)
HCN (ice)	8.5(-9)	2.1(-8)	3.5(-8)
HNC	7.9(-10)	1.2(-8)	3.8(-10)
HNC (ice)	5.4(-11)	3.0(-9)	9.8(-9)
CN	3.5(-8)	4.4(-9)	9.6(-12)
HCO <sup>+</sup>	3.3(-11)	1.4(-9)	7.8(-10)
CO	9.0(-6)	3.6(-5)	5.9(-6)
CO (ice)	3.0(-7)	9.3(-6)	4.2(-5)
CS	8.4(-10)	1.9(-9)	1.2(-10)
CS (ice)	2.1(-14)	2.2(-14)	2.2(-14)
SO	8.1(-14)	1.4(-12)	6.7(-11)
SO (ice)	4.5(-14)	6.7(-13)	6.9(-11)
H <sub>2</sub> S (ice)	7.0(-8)	7.6(-8)	7.8(-8)
N <sub>2</sub> H <sup>+</sup>	2.9(-11)	6.9(-11)	7.0(-11)
N <sub>2</sub> (ice)	1.9(-7)	2.0(-6)	6.3(-6)
NH <sub>3</sub> (ice)	2.6(-6)	4.8(-6)	6.5(-6)
NO	2.0(-9)	3.1(-9)	8.4(-8)
NO (ice)	8.4(-11)	8.1(-10)	1.3(-7)
H <sub>3</sub> O <sup>+</sup>	6.9(-11)	1.7(-9)	3.9(-10)
H <sub>2</sub> O	9.2(-9)	2.9(-7)	8.9(-8)
H <sub>2</sub> O (ice)	2.9(-5)	7.3(-5)	1.2(-4)
H <sub>2</sub> CO	9.8(-10)	3.5(-10)	2.4(-10)
H <sub>2</sub> CO (ice)	1.0(-10)	5.4(-9)	3.8(-8)
SiO	6.2(-12)	1.4(-11)	1.7(-12)
SiH <sub>4</sub> (ice)	7.6(-9)	7.9(-9)	7.9(-9)
HC <sub>3</sub> N	5.3(-14)	2.8(-11)	4.8(-11)
HC <sub>3</sub> N (ice)	2.0(-15)	2.1(-12)	2.1(-10)
CH <sub>4</sub> (ice)	6.5(-6)	2.0(-5)	2.2(-5)

**Table 5.** Pre-shock fractional abundances of observed species and other related species in different pre-shock densities of  $n = 2 \times 10^4 \text{ cm}^{-3}$ ,  $2 \times 10^5 \text{ cm}^{-3}$ , and  $2 \times 10^6 \text{ cm}^{-3}$ . Species on grain surfaces are indicated with "(ice)" while species without any note mean that they are in the gas phase. A value of  $a \times 10^{-b}$  is expressed as a(-b).

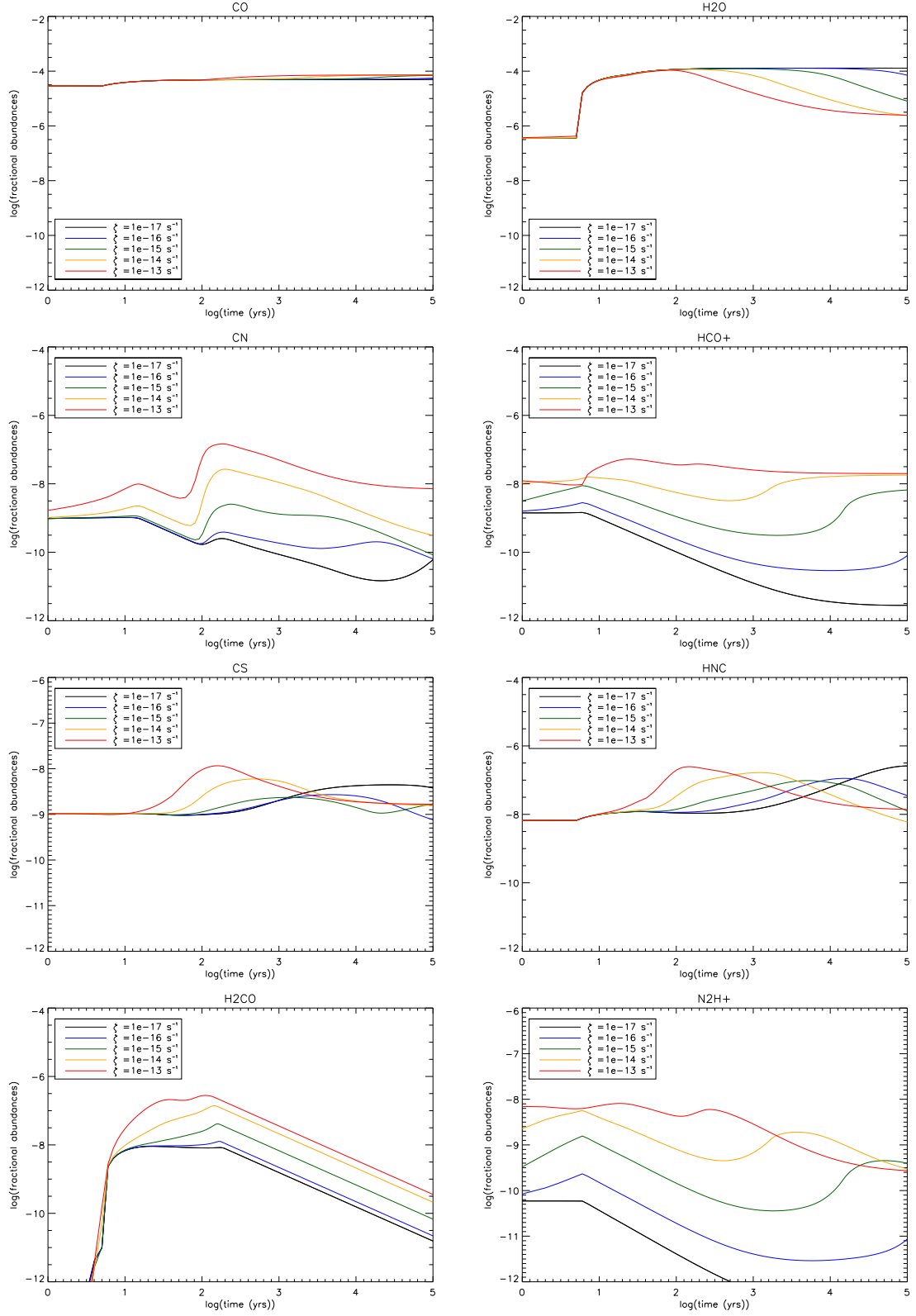


**Fig. 5.** Time-averaged fractional abundances of observed species are shown for  $n_H = 2 \times 10^5 \text{ cm}^{-3}$ ,  $v = 20 \text{ km s}^{-1}$ , and varying cosmic-ray ionization rates of  $\zeta = 1 \times 10^{-17} \text{ s}^{-1} - 1 \times 10^{-13} \text{ s}^{-1}$ .

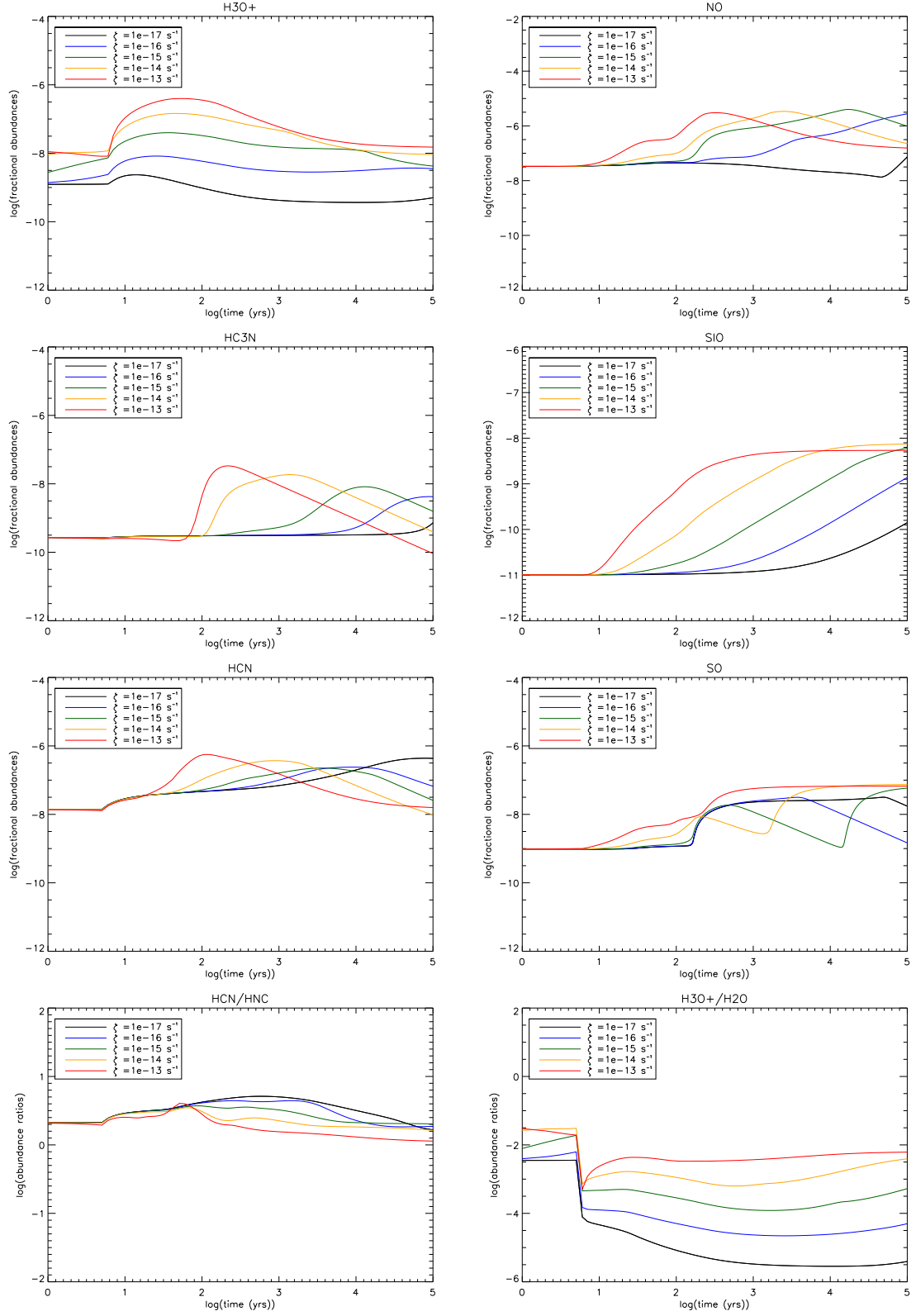


**Fig. 6.** Same as Figure 7, but for other different species. The bottom panels are showing the abundance ratios instead of fractional abundances.

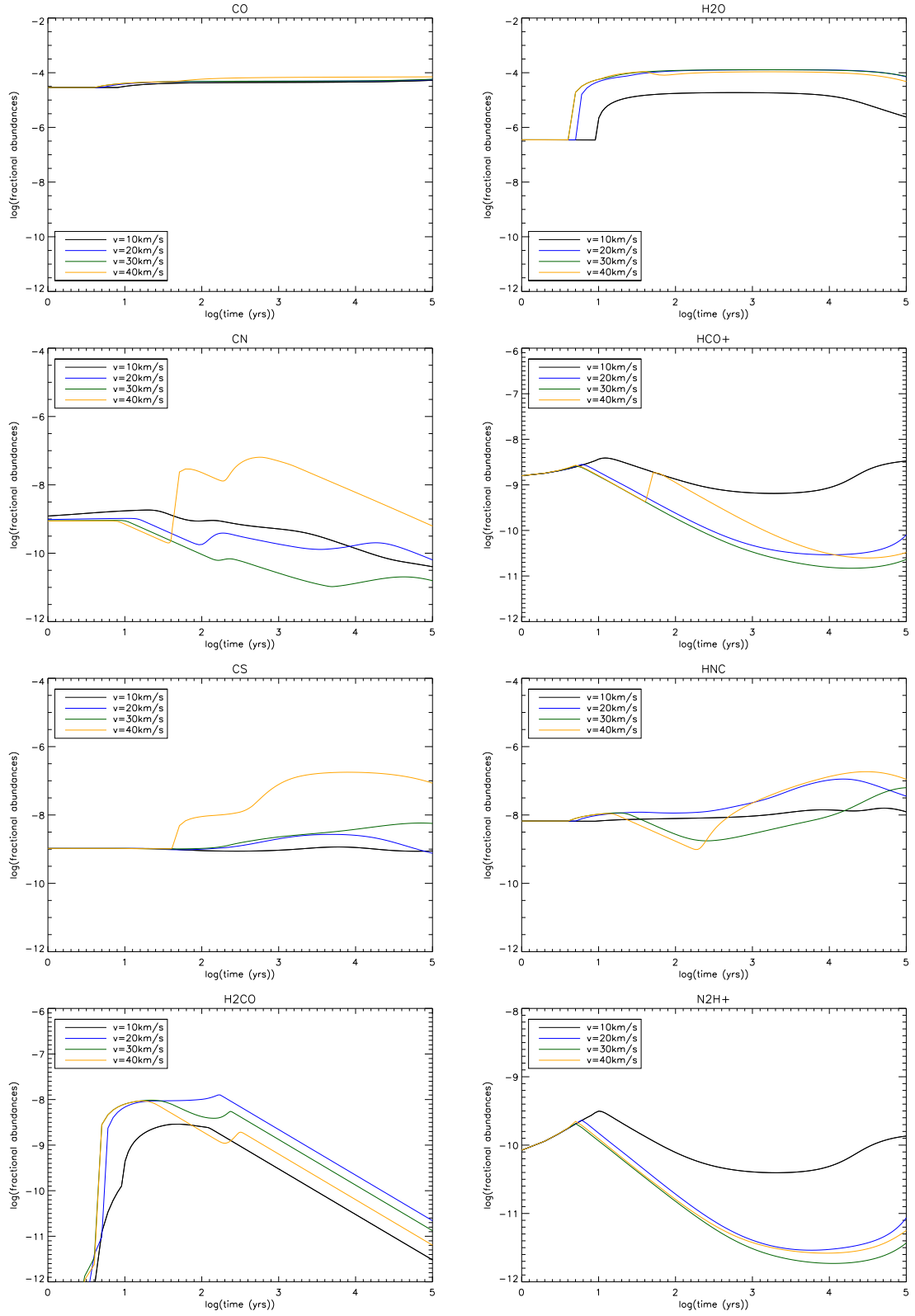


**Fig. 7.** Time-averaged fractional abundances of observed species are shown for  $n = 10^5 \text{ cm}^{-3}$ , a cosmic-ray ionization rate of  $\zeta = 1 \times 10^{-16} \text{ s}^{-1}$ , with varying shock velocities of 10, 20, 30, and 40  $\text{km s}^{-1}$ .

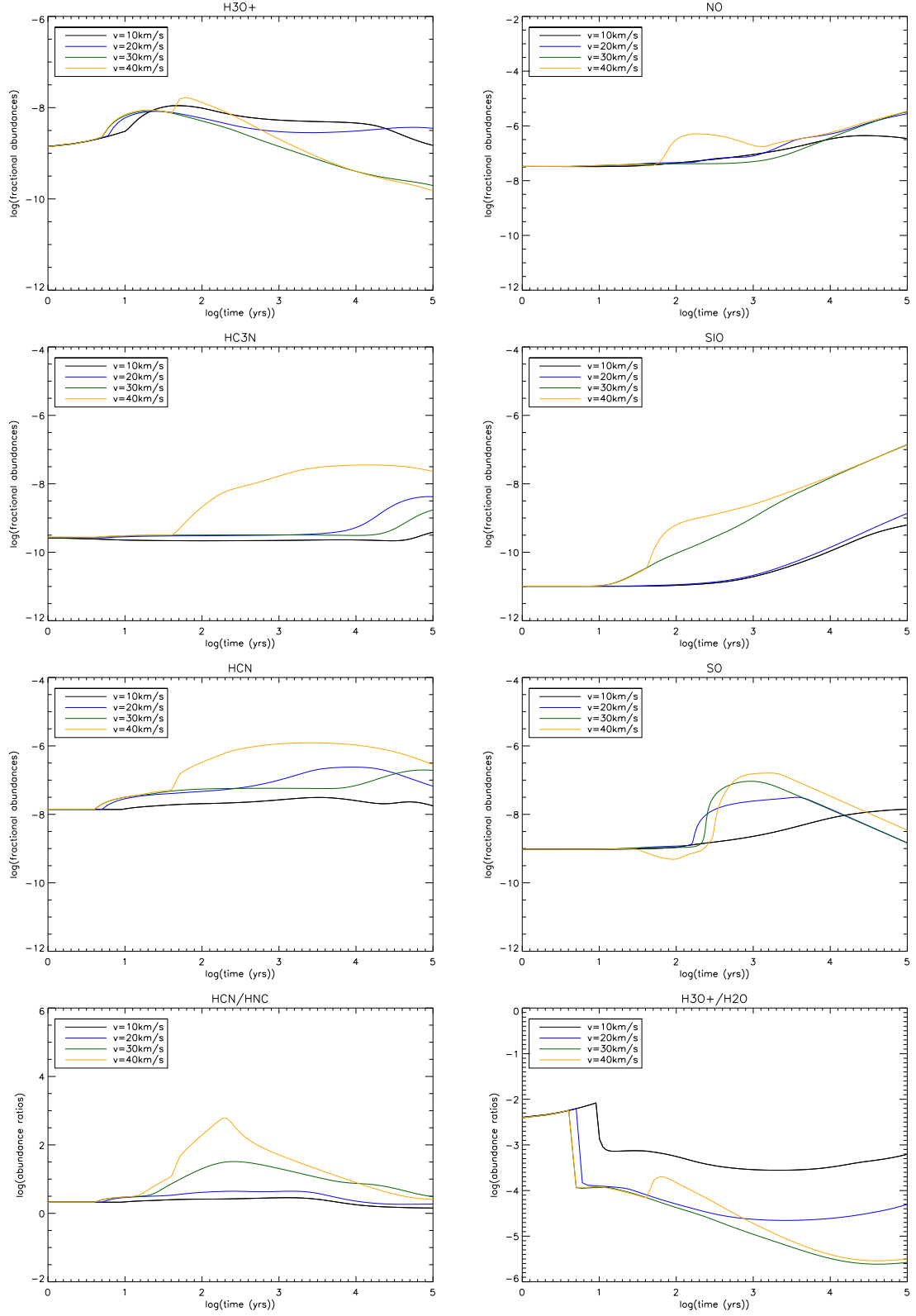


**Fig. 8.** Same as Figure 7, but for different species. The bottom panels are showing the abundance ratios instead of fractional abundances.

**Acknowledgements.** NH thanks Miwa Goto for sharing her results on X-ray ionization rate in her paper. IJ-S acknowledges funding from the People Programme (Marie Curie Actions) of the European Union's Seventh Framework Programme (FP7/2007-2013) under REA grant agreement number PIIF-GA-2011-301538.

## References

- Amo-Baladrón, M. A., Martín-Pintado, J., & Martín, S. 2011, *A&A*, 526, A54  
Anders, E. & Grevesse, N. 1989, *Geochim. Cosmochim. Acta*, 53, 197  
Ao, Y., Henkel, C., Menten, K. M., et al. 2013, *A&A*, 550, A135  
Baganoff, F. K., Maeda, Y., Morris, M., et al. 2003, *ApJ*, 591, 891  
Bradford, C. M., Stacey, G. J., Nikola, T., et al. 2005, *ApJ*, 623, 866  
Capelli, R., Warwick, R. S., Porquet, D., Gillessen, S., & Predehl, P. 2012, *A&A*, 545, A35  
Chernyakova, M., Malyshev, D., Aharonian, F. A., Crocker, R. M., & Jones, D. I. 2011, *ApJ*, 726, 60  
Christopher, M. H., Scoville, N. Z., Stolovy, S. R., & Yun, M. S. 2005, *ApJ*, 622, 346  
Dalgarno, A., Yan, M., & Liu, W. 1999, *ApJS*, 125, 237  
Flower, D. R. & Pineau des Forêts, G. 2012, *MNRAS*, 421, 2786  
Foster, A. R., Ji, L., Smith, R. K., & Brickhouse, N. S. 2012, *ApJ*, 756, 128  
Garrod, R. T., Wakelam, V., & Herbst, E. 2007, *A&A*, 467, 1103  
Goto, M., Geballe, T. R., Indriolo, N., et al. 2014, *ApJ*, 786, 96  
Goto, M., Indriolo, N., Geballe, T. R., & Usuda, T. 2013, *Journal of Physical Chemistry A*, 117, 9919  
Goto, M., Usuda, T., Nagata, T., et al. 2008, *ApJ*, 688, 306  
Graedel, T. E., Langer, W. D., & Frerking, M. A. 1982, *ApJS*, 48, 321  
Graninger, D. M., Herbst, E., Öberg, K. I., & Vasyunin, A. I. 2014, *ApJ*, 787, 74  
Gusdorf, A., Cabrit, S., Flower, D. R., & Pineau Des Forêts, G. 2008, *A&A*, 482, 809  
Güsten, R., Genzel, R., Wright, M. C. H., et al. 1987, *ApJ*, 318, 124  
Güsten, R., Nyman, L. Å., Schilke, P., et al. 2006, *A&A*, 454, L13  
Indriolo, N., Fields, B. D., & McCall, B. J. 2009, *ApJ*, 694, 257  
Jiménez-Serra, I., Caselli, P., Martín-Pintado, J., & Hartquist, T. W. 2008, *A&A*, 482, 549  
Kasemann, C., Güsten, R., Heyminck, S., et al. 2006, in *Society of Photo-Optical Instrumentation Engineers (SPIE) Conference Series*, Vol. 6275, Society of Photo-Optical Instrumentation Engineers (SPIE) Conference Series  
Klein, T., Ciechanowicz, M., Leinz, C., et al. 2014, *IEEE Trans. on Terahertz Science and Technology*, 4, 588  
Koyama, K., Hyodo, Y., Inui, T., et al. 2007, *PASJ*, 59, 245  
Lacy, J. H., Townes, C. H., Geballe, T. R., & Hollenbach, D. J. 1980, *ApJ*, 241, 132  
Le Petit, F., Nehmé, C., Le Boulrot, J., & Roueff, E. 2006, *ApJS*, 164, 506  
Linden, T., Lovegrove, E., & Profumo, S. 2012, *ApJ*, 753, 41  
Lo, K. Y. 1986, *Science*, 233, 1394  
Martín, S., Martín-Pintado, J., Montero-Castaño, M., Ho, P. T. P., & Blundell, R. 2012, *A&A*, 539, A29  
Martín-Pintado, J., de Vicente, P., Fuente, A., & Planesas, P. 1997, *ApJ*, 482, L45  
Mills, E. A. C., Güsten, R., Requena-Torres, M. A., & Morris, M. R. 2013, *ApJ*, 779, 47  
Montero-Castaño, M., Herrnstein, R. M., & Ho, P. T. P. 2009, *ApJ*, 695, 1477  
Morton, D. C. 1974, *ApJ*, 193, L35  
Nobukawa, M., Koyama, K., Tsuru, T. G., Ryu, S. G., & Tatischeff, V. 2010, *PASJ*, 62, 423  
Oka, T., Nagai, M., Kamegai, K., & Tanaka, K. 2011, *ApJ*, 732, 120  
Padovani, M., Galli, D., & Glassgold, A. E. 2009, *A&A*, 501, 619  
Paumard, T., Genzel, R., Martins, F., et al. 2006, *ApJ*, 643, 1011  
Ponti, G., Morris, M. R., Terrier, R., & Goldwurm, A. 2013, in *Advances in Solid State Physics*, Vol. 34, *Cosmic Rays in Star-Forming Environments*, ed. D. F. Torres & O. Reimer, 331  
Ponti, G., Terrier, R., Goldwurm, A., Belanger, G., & Trap, G. 2010, *ApJ*, 714, 732  
Prasad, S. S. & Tarafdar, S. P. 1983, *ApJ*, 267, 603  
Reid, M. J., Menten, K. M., Zheng, X. W., et al. 2009, *ApJ*, 700, 137  
Requena-Torres, M. A., Güsten, R., Weiß, A., et al. 2012, *A&A*, 542, L21  
Requena-Torres, M. A., Martín-Pintado, J., Martín, S., & Morris, M. R. 2008, *ApJ*, 672, 352  
Requena-Torres, M. A., Martín-Pintado, J., Rodríguez-Franco, A., et al. 2006, *A&A*, 455, 971  
Revnivtsev, M. G., Churazov, E. M., Sazonov, S. Y., et al. 2004, *A&A*, 425, L49  
Roberts, J. F., Rawlings, J. M. C., Viti, S., & Williams, D. A. 2007, *MNRAS*, 382, 733  
Sakai, N., Sakai, T., Hirota, T., & Yamamoto, S. 2008, *ApJ*, 672, 371  
Schilke, P., Walmsley, C. M., Pineau des Forêts, G., & Flower, D. R. 1997, *A&A*, 321, 293  
Schödel, R., Merritt, D., & Eckart, A. 2009, *A&A*, 502, 91

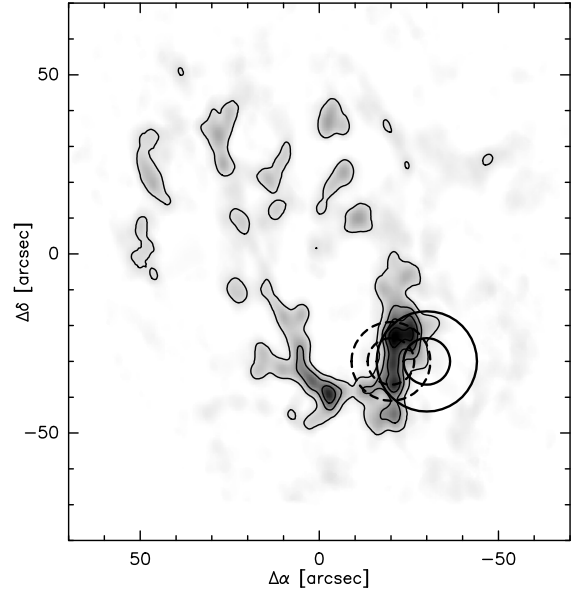


**Fig. 1.** A contour map of HCN (4-3) emission in the CND from Montero-Castaño et al. (2009). Circles in solid lines show minimum and maximum beam sizes for the IRAM 30m telescope, and circles in dotted lines are for APEX FLASH instrument. The central position is the location of Sgr A\* at EQ J2000  $\alpha = 17:45:39.99$ ,  $\delta = -29:00:26.6$ . One arcsecond corresponds to 0.04 pc using the distance to the Galactic Center as  $d = 8.4$  kpc

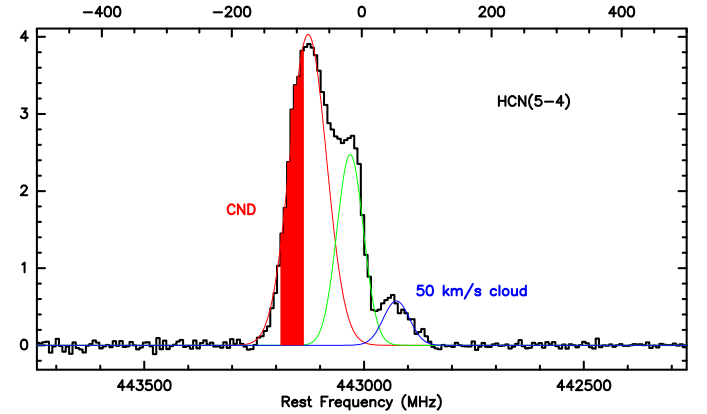


**Fig. 2.** A spectrum of HCN(5-4) is shown as an example of typical velocity components in the line of sight. A component centered at  $\sim 50$  km s<sup>-1</sup> is from “50 km s<sup>-1</sup> cloud,” whereas other two components are from the CND. The velocity range used for the analysis, which should come from a cloud in the southwest lobe, is highlighted.

- Serabyn, E., Guesten, R., Walmsley, J. E., Wink, J. E., & Zylka, R. 1986, *A&A*, 169, 85  
Smith, I. L. & Wardle, M. 2014, *MNRAS*, 437, 3159  
Takekawa, S., Oka, T., Tanaka, K., et al. 2014, *ApJS*, 214, 2  
Terrier, R., Ponti, G., Bélanger, G., et al. 2010, *ApJ*, 719, 143  
Tielens, A. G. G. M. 2005, *The Physics and Chemistry of the Interstellar Medium* (Cambridge University Press)  
van der Tak, F. F. S., Belloche, A., Schilke, P., et al. 2006, *A&A*, 454, L99  
van der Tak, F. F. S., Black, J. H., Schöier, F. L., Jansen, D. J., & van Dishoeck, E. F. 2007, *A&A*, 468, 627  
Viti, S., Collings, M. P., Dever, J. W., McCoustra, M. R. S., & Williams, D. A. 2004, *MNRAS*, 354, 1141  
Viti, S., Jiménez-Serra, I., Yates, J. A., et al. 2011, *ApJ*, 740, L3

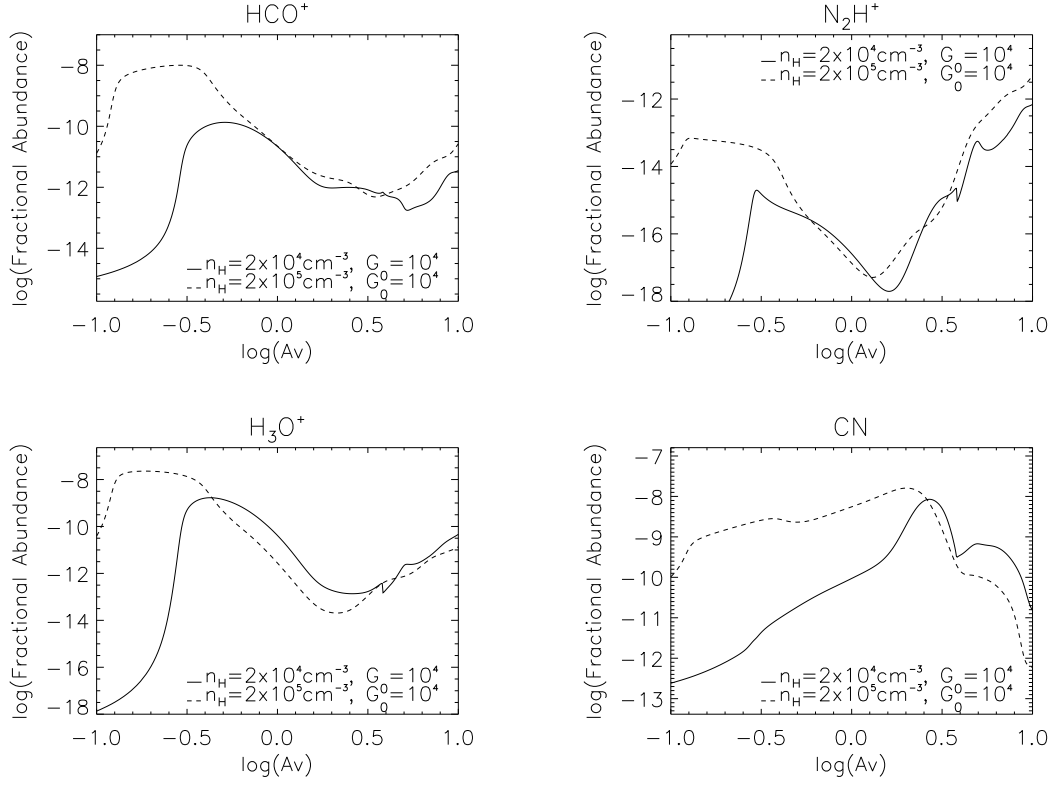


**Fig. 9.** Fractional abundances of  $\text{HCO}^+$ ,  $\text{N}_2\text{H}^+$ ,  $\text{H}_3\text{O}^+$ , and  $\text{CN}$  derived by Meudon PDR code for  $n_H = 2 \times 10^4$  and  $2 \times 10^5 \text{ cm}^{-3}$ ,  $G_0 = 10^4$ , and  $\zeta = 1 \times 10^{-17} \text{ s}^{-1}$ .

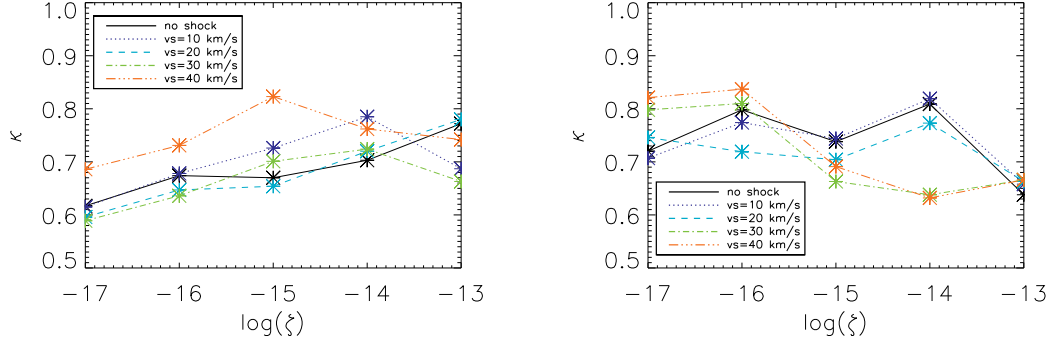


**Fig. 10.** Values of confidence level as a function of cosmic-ray ionization rate are shown for  $n_H = 2 \times 10^5 \text{ cm}^{-3}$  (left panel) and  $n_H = 2 \times 10^4 \text{ cm}^{-3}$  (right panel).

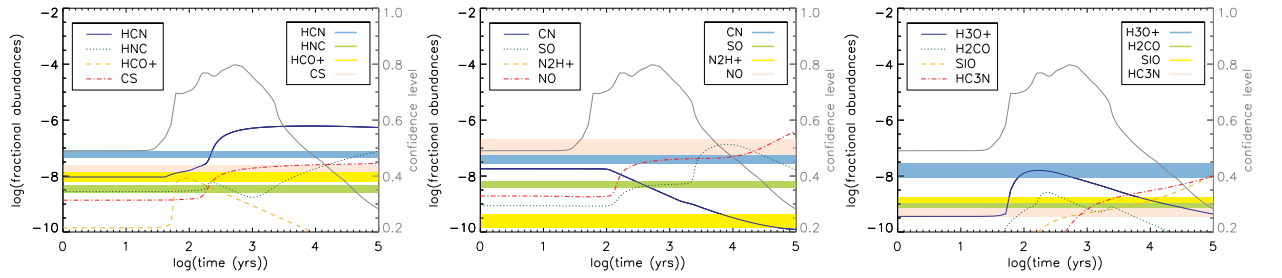


**Fig. 11.** Time-averaged fractional abundances  $\langle X(t) \rangle = \int X(t') dt' / t$  are shown for  $n_H = 2 \times 10^4 \text{ cm}^{-3}$ ,  $\zeta = 10^{-17} \text{ s}^{-1}$ , and  $v_s = 30 \text{ km s}^{-1}$  with solid lines. Observed abundance ratios over CO are shown as filled colors. The grey line with the right ordinate scale shows the value of confidence level as a function of time.



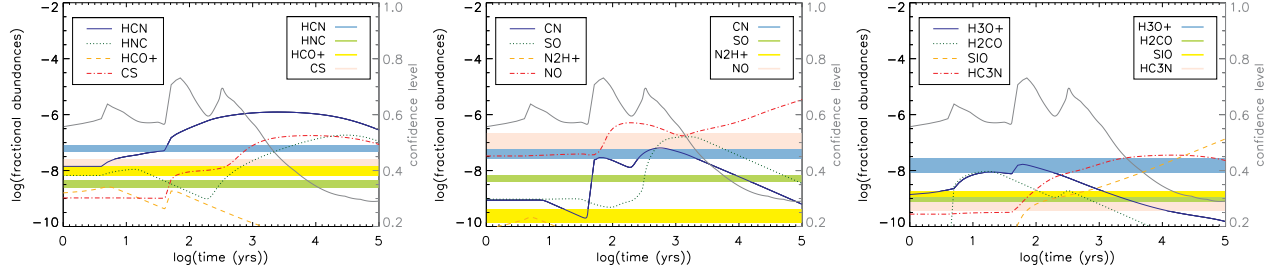


**Fig. 12.** Same as Figure 11 for  $n_H = 2 \times 10^5 \text{ cm}^{-3}$ ,  $\zeta = 10^{-16} \text{ s}^{-1}$ , and  $v_s = 40 \text{ km s}^{-1}$ .

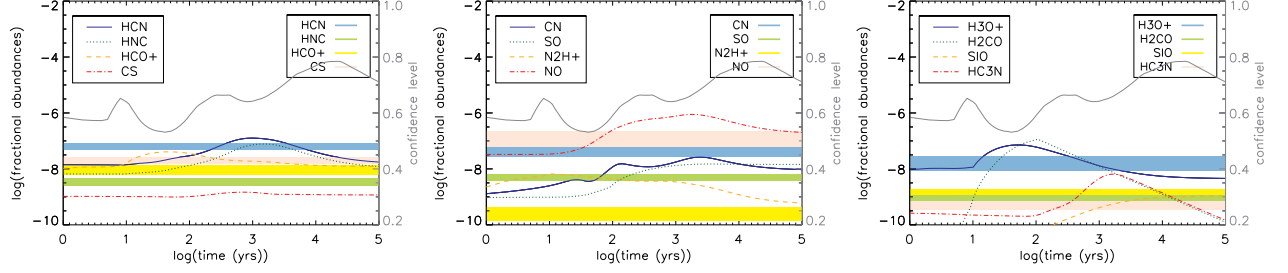


**Fig. 13.** Same as Figure 11 for  $n_H = 2 \times 10^5 \text{ cm}^{-3}$ ,  $\zeta = 10^{-14} \text{ s}^{-1}$ , and  $v_s = 10 \text{ km s}^{-1}$ .

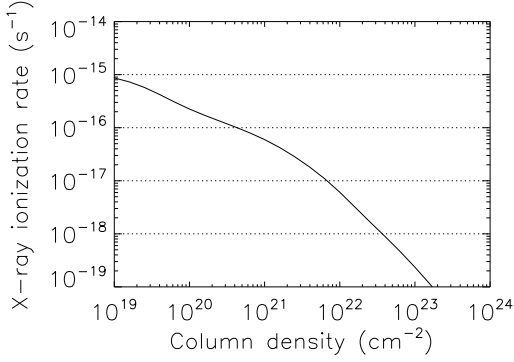


**Fig. 4.** The solid line shows the X-ray ionization rate derived by using a current X-ray luminosity  $L_X = 2 \times 10^{33} \text{ erg s}^{-1}$  in 2-10 keV range (Baganoff et al. 2003) as a function of intervening column density at a distance of  $d = 2 \text{ pc}$  from the X-ray source. X-ray flux in lower energy range is estimated by AtomDB program (Foster et al. 2012) following a similar procedure in Goto et al. (2013) using a plasma temperature of  $kT = 1.9 \text{ keV}$ .

- Wakelam, V. & Herbst, E. 2008, *ApJ*, 680, 371  
 Woodall, J., Agúndez, M., Markwick-Kemper, A. J., & Millar, T. J. 2007, *A&A*, 466, 1197  
 Yusef-Zadeh, F., Cotton, W., Viti, S., Wardle, M., & Royster, M. 2013a, *ApJ*, 764, L19  
 Yusef-Zadeh, F., Hewitt, J. W., Wardle, M., et al. 2013b, *ApJ*, 762, 33  
 Yusef-Zadeh, F., Munro, M., Wardle, M., & Lis, D. C. 2007, *ApJ*, 656, 847